metals

MDPI

Article

Optimizing Heat Treatment to Improve the Microstructures and Mechanical Properties of 5CrNiMoV Steel

Wanhui Huang, Liping Lei and Gang Fang *

State Key Laboratory of Tribology in Advanced Equipment (SKLT), Department of Mechanical Engineering, Tsinghua University, Beijing 100084, China; huangwh17@tsinghua.org.cn (W.H.)
* Correspondence: fangg@tsinghua.edu.cn

Abstract: A strategy combining intercritical quenching, pre-tempering, and tempering processes was implemented to optimize the microstructures and mechanical properties of 5CrNiMoV steel. By intercritically quenching at 1050 °C, pr-tempering at 600 °C, and tempering at 550 °C, the steel exhibited a comprehensive performance with a yield strength of 1120 MPa, an ultimate tensile strength of 1230 MPa, and an elongation of 8.2%. The high strength of the steel is attributed to the presence of tempered martensite and abundant secondary carbides. The favorable ductility is mainly provided by the pearlite inherited from intercritical quenching and tempering. Additionally, the precipitation of secondary carbides not only enhances precipitation strengthening, but also reduces the dislocation density and lattice strain of the matrix, thereby enhancing strength and ductility. This study offers a scheme for producing strong and ductile 5CrNiMoV steel.

Keywords: heat treatment; microstructure; 5CrNiMoV; die steel; precipitation

check for updates

Citation: Huang, W.; Lei, L.; Fang, G. Optimizing Heat Treatment to Improve the Microstructures and Mechanical Properties of 5CrNiMoV Steel. *Metals* **2023**, *13*, 1263. https://doi.org/10.3390/met13071263

Academic Editor: Koh-ichi Sugimoto

Received: 28 June 2023
Revised: 9 July 2023
Accepted: 10 July 2023
Published: 13 July 2023

1. Introduction

5CrNiMoV is a low alloy martensitic die steel that is commonly used in the manufacturing of tools for forging, extrusion, and die-casting processes [1,2]. Tools made from this steel are exposed to high pressure, friction, and multiple thermal cycles during the hot forming of materials. These harsh operating conditions often lead to a limited lifespan for tools [3,4]. Therefore, it is necessary to enhance the mechanical properties of 5CrNiMoV steel.

As is well known, the microstructure of steel and alloys plays a crucial role in determining their mechanical properties, and this is widely recognized. In the case of 5CrNiMoV steel, the microstructure typically consists of martensite and dispersed secondary carbides that are formed during the process of quenching-tempering (QT) heat treatment. It is important to note that the type, morphology, distribution, and average size of these secondary carbides significantly impact the operational lifespan and reliability of the die steel [4–6].

In recent years, several researchers have investigated the impact of heat treatment on the microstructure and secondary carbides of die steels, as well as its effect on their mechanical properties [7–10]. During the QT treatment, the prior austenite grain size (PAGS) and volume fraction of carbides are influenced by the quenching temperature, while the martensite morphology and secondary carbides size are influenced by the tempering temperature [7]. It has been observed that increasing the tempering temperature leads to the precipitation and coarsening of spherical carbides in the martensite lath [8]. Additionally, Zhu et al. [9] proposed that the pre-tempering process can refine the tempered martensite and carbides of H13 die steel. The findings indicate that fine grains, lath martensite, and carbides contribute to the ductility and strength of H13 die steel [9,10].

Moreover, recent research has reported that steel containing a microstructure consisting of at least two distinct transformation products can attain both high strength and high ductility [11–13]. Sun et al. [11] demonstrated that a layered structure of martensite and

ultrafine-grained ferrite can circumvent the strength-toughness trade-off typically observed in low-alloyed steel. The findings reveal that in comparison to a tempered martensitic microstructure, the martensite and ultrafine-grained ferrite layered microstructure exhibit a significant enhancement in impact toughness. Furthermore, He et al. [12] and Li et al. [13] successfully developed medium-manganese steels featuring a refined austenite and martensite structure. This advanced medium-manganese steel boasts an ultimate tensile strength exceeding 2000 MPa and an elongation surpassing 20%.

Gaining a comprehensive understanding of the microstructural evolution of 5CrNiMoV steel is of paramount importance. However, limited efforts have been made to elucidate the methodology for controlling the tempered martensitic microstructure in 5CrNiMoV steel. Consequently, this study aims to propose an optimal heat treatment route to enhance its microstructures and mechanical properties. An intercritical quenching process—followed by high-temperature pre-tempering and low-temperature tempering—is developed. Furthermore, employing optical microscope (OM) and scanning electron microscope (SEM) observations, along with X-ray diffraction (XRD) and energy dispersive spectroscopy (EDS) analyses, the microstructure evolution and precipitation behavior of secondary carbides during the heat treatment of 5CrNiMoV steel are thoroughly examined and discussed.

2. Materials and Methods

2.1. Materials

Table 1 lists the chemical compositions of the 5CrNiMoV die steel, which was taken from an as-forged billet.

Table 1. Chemical compositions of the 5CrNiMoV steel (wt.%).

Element	C	Si	Mn	Cr	Ni	Mo	V	P	S
wt.%	0.54	0.25	0.72	0.96	1.58	0.36	0.074	0.012	0.003

Phase transformation temperatures of the 5CrNiMoV steel were investigated using differential scanning calorimetry (DSC) measurements (STA 449F3 Jupiter). During the measurement, the specimen was heated from 25 °C to 1100 °C at a rate of 10 °C/s, and the heat flow rate to the specimen was monitored. In addition, a quenching and deformation dilatometer (DIL 805, TA instruments, New Castle, DE, USA) was used to carry out the thermal expansion tests of the steel. The specimens used for the thermal expansion test are 10 mm in height and 4 mm in diameter. During the test, the specimens were heated to 950 °C, 1050 °C, and 1100 °C, respectively, at a heating rate of 10 °C/s, kept for 5 min, and then cooled at a linear rate of 50 °C/s. The results of the dilatometer tests show that the M_s temperature is 240 °C and the M_f is lower than room temperature.

2.2. Heat Treatment Process

Firstly, the specimens were heated to either 1050 °C or 1100 °C and held at these temperatures for 30 min. Subsequently, they were quenched in oil, as shown in Figure 1a. After the quenching process, the specimens underwent pre-tempering and tempering treatments. In the pre-tempering stage, the specimen was reheated to a temperature of either 550 or 600 °C and hold for 120 min, followed by air cooling. Subsequently, the specimen was reheated to a temperature that was equal to or lower than the pre-tempering temperature (550 or 600 °C). Then, an intercritical quenching method was proposed to produce a mixed structure of pearlite and martensite in the 5CrNiMoV steel. This method involves quenching the specimen after isothermal holding at 1050 °C for 30 min. The quenching process was performed by rapidly immersing the specimen into a quenching oil at a temperature of about 100 °C for a duration of 10 s. Subsequently, the intercritically quenched specimen underwent pre-tempering and tempering treatments, as shown in Figure 1b.

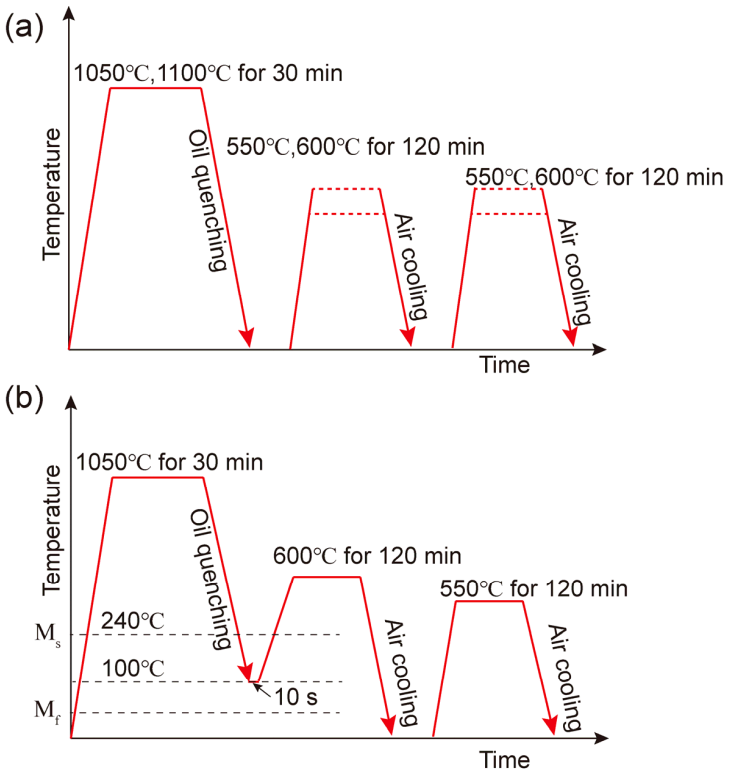

Figure 1. Schematic diagrams of heat treatments: (**a**) quenching and tempering, (**b**) intercritical quenching and tempering.

Additionally, the strength of 5CrNiMoV steel is influenced by precipitation strengthening, which is caused by the formation of secondary carbides. To determine the appropriate tempering conditions, the researchers referred to the equilibrium phase diagram of the 5CrNiMoV steel, as depicted in Figure 2. It was observed that due to the low silicon content, the formation of cementite is more favorable compared to other carbides [14]. However, in terms of contributing to the strength of the die steel, the carbides MC and $M_{23}C_6$ play a more significant role than cementite. Based on the information provided in Figure 2, it was found that the carbides $M_{23}C_6$ and MC remain stable within the temperature range of 550 °C to 650 °C. Therefore, for this research, the tempering temperature was selected from a range of 550 °C to 600 °C.

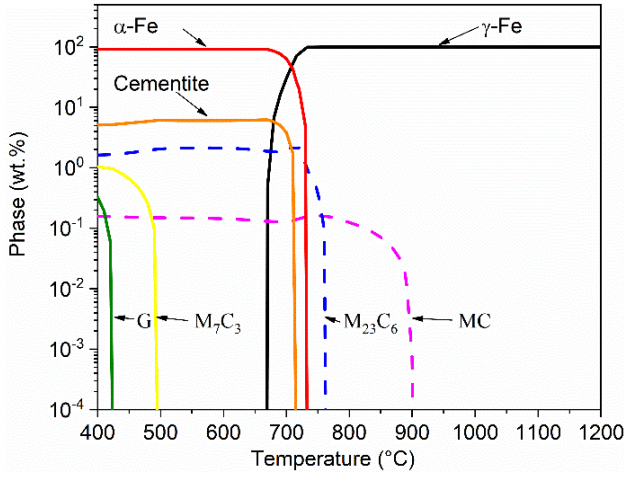

Figure 2. Equilibrium phase diagram of the 5CrNiMoV steel (calculated using JMatPro V. 7.0 software).

2.3. Microstructure and Mechanical Properties Characterization

The experimental setup for the tensile tests and the dimensions of the tensile specimens are shown in Figure 3. Two tensile specimens were prepared for each heat-treated sample. The tensile tests were conducted at room temperature using a material testing machine (Shimadzu AGX-V) with a loading rate of 0.005 mm/s. To accurately measure the strain of the tensile specimen, the digital image correlation method was employed [15]. The resolution of the camera was 300 × 1000 = 300,000 pixels. The hardness of the quenched specimens was tested using a Rockwell hardness tester (HRS-150).

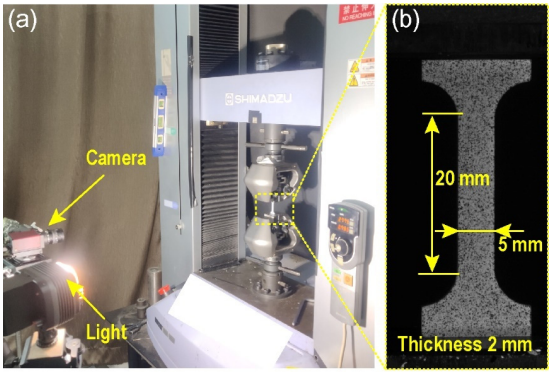

Figure 3. (**a**) Tensile testing equipment; (**b**) dimensions of the tensile specimen.

The microstructures of the specimens were examined using an OM (Zeiss, Jena, Germany, Axio Observer Z1M) and an SEM (Zeiss, Sigma 300) equipped with an EDS system. Prior to observations, all specimens were mechanically polished, ground, and subsequently chemically etched using 4% nital. Furthermore, the micro-strain and dislocation of the heat-treated specimens were estimated by the XRD (Bruker, Billerica, MA, USA, D8 Discover). The size and volume fraction of carbides were measured using Image-Pro Plus software.

3. Results and Discussion

3.1. Dissolution of Carbides

As shown in Figure 4a, the transformation temperatures of Ac_1 (750 °C) and Ac_3 (770 °C) of the 5CrNiMoV steel were determined according to the heating dilatation curve. The DSC curve, shown in Figure 4b, exhibits two endothermic valleys. Previous studies have reported that the transformation of ferrite to austenite, carbide dissolution, and grain growth are all endothermic processes [16,17]. Therefore, the first endothermic valley in the DSC curve corresponds to the austenite transformation, while the second one corresponds to the grain growth and dissolution of carbides.

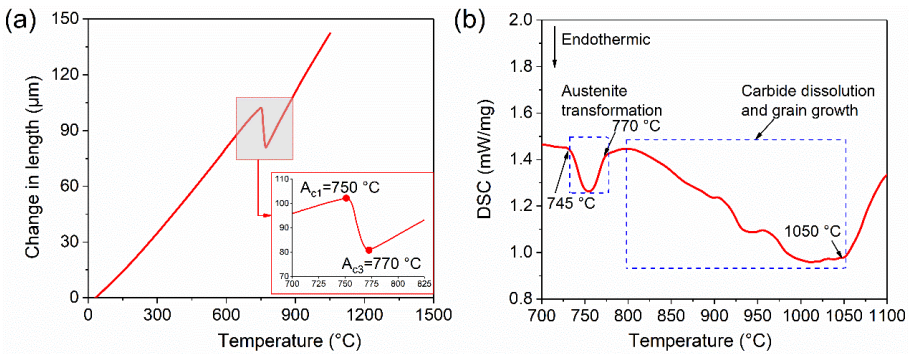

Figure 4. Transformation temperatures test. (**a**) The dilatometry curve and (**b**) the DSC curve of the 5CrNiMoV steel.

It is worth noting that the DSC curve does not exhibit an exothermic reaction until the temperature reaches approximately 1050 °C. This suggests that the complete dissolution of carbides only occurs when the temperature reaches 1050 °C.

Figure 5 displays the martensite of specimens quenched at various temperatures. As illustrated in Figure 5a, undissolved particles can be observed on the martensite matrix of the specimen quenched at 950 °C, as indicated by the yellow arrows. To further investigate these particles, the chemical element variations along the line crossing them were characterized using EDS, as shown in Figure 5b. The results reveal that the undissolved particle is a chromium (Cr) -rich carbide. In contrast, no such undissolved particles are observed in Figure 5c,d for specimens quenched at 1050 °C and 1100 °C, respectively.

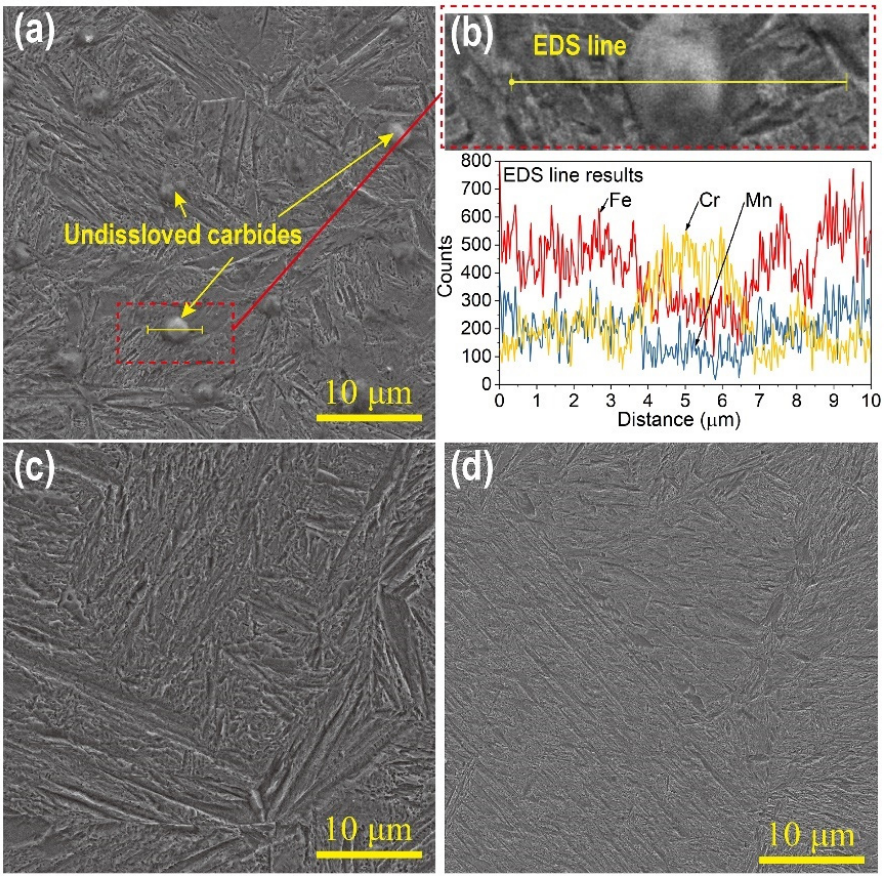

Figure 5. SEM micrographs of the 5CrNiMoV steel quenched at (**a**) 950 °C, (**c**) 1050 °C, and (**d**) 1100 °C. (**b**) EDS line results of the particle in (**a**).

The presence of undissolved Cr-rich carbide reduces the chromium content in the matrix structure, leading to an inhomogeneous microstructure. This inhomogeneity is detrimental to the strength of steel. As depicted in Figure 6, the specimen quenched at 950 °C exhibits the lowest hardness, measuring at (52 ± 1) HRC. This decrease in hardness is attributed to the undissolved carbides (Figure 5a), which reduce the alloying elements within the quenching martensite, consequently resulting in a decrease in martensitic hardness. Upon quenching at 1050 °C, the martensitic hardness reaches its peak, measuring at (59 ± 1) HRC. However, when quenched at 1100 °C, the hardness declines to (57 ± 1) HRC. This reduction in hardness is associated with excessive quenching temperature, which leads to the coarsening of prior austenite grains and subsequently decreases the hardness of the specimen. The results indicate that the presence of undissolved Cr-rich carbides in specimens quenched at lower temperatures results in an inhomogeneous microstructure and a decrease in hardness. Conversely, excessive quenching temperature causes prior

austenite grain coarsening and a subsequent decline in hardness. Therefore, a quenching temperature of 1050 °C is considered reasonable for 5CrNiMoV steel.

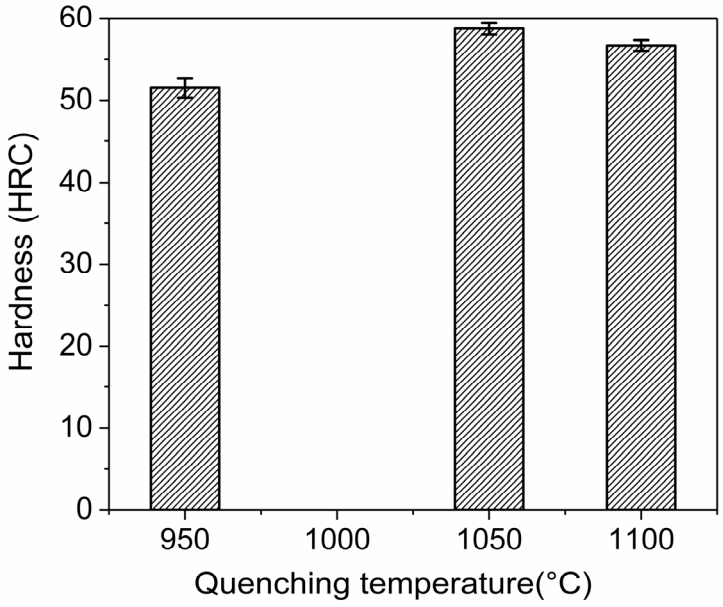

Figure 6. Martensitic hardness of the 5CrNiMoV steel quenched at different temperatures.

3.2. Mechanical Properties

The engineering stress-strain curves of the heat-treated specimens are depicted in Figure 7. Furthermore, the ultimate tensile strength (UTS), yield strength (YS), and elongation to rupture (EL) of various specimens are provided in Table 2. The numbers in the legend denote the conditions of heat treatment. For instance, 1050-550-550 signifies that the quenching, pre-tempering, and tempering temperatures are 1050 °C, 550 °C, and 550 °C, respectively. Moreover, 1050L-600-550 indicates the implementation of intercritical quenching, where the specimen was intercritically quenched at 1050 °C, followed by pre-tempering at 600 °C and tempering at 550 °C.

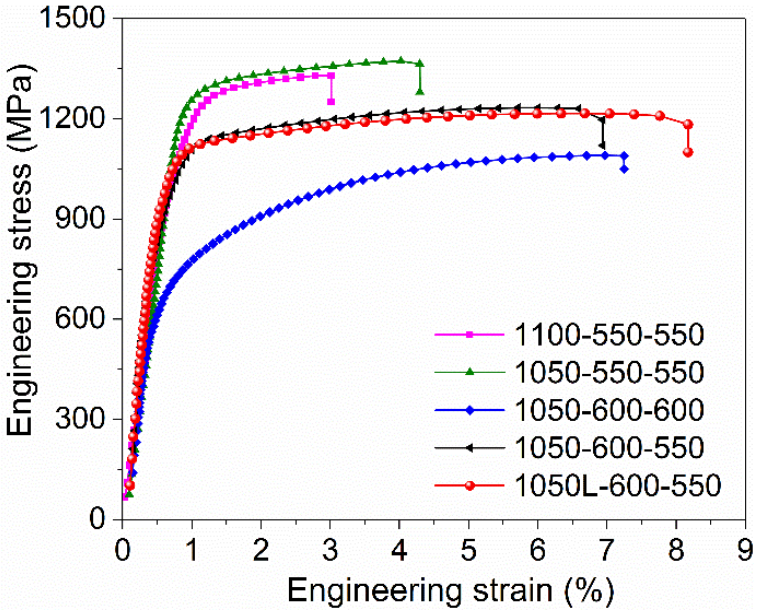

Figure 7. Engineering stress-strain curves of different heat-treated specimens.

Table 2. Tensile properties of the 5CrNiMoV steel heat-treated under different conditions.

Specimen	UTS (MPa)	YS (MPa)	EL (%)
1100-550-550	1330 ± 15	1200 ± 15	3.0 ± 0.5
1050-550-550	1375 ± 25	1290 ± 12	4.0 ± 0.8
1050-600-600	1090 ± 10	670 ± 8	7.0 ± 0.6
1050-600-550	1230 ± 20	1120 ± 10	7.0 ± 0.5
1050L-600-550	1220 ± 16	1110 ± 10	8.2 ± 0.3

Specimen (S) 1050-550-550 demonstrates superior strength and ductility compared to S1100-550-550. It is observed that with an increase in quenching temperature, the UTS and YS decline from 1375 MPa to 1330 MPa and 1290 MPa to 1200 MPa, respectively. Simultaneously, the EL decreases from 4.0% to 3.0%. This can be attributed to two factors. Firstly, the PAGS and martensite block size augment with an increase in quenching temperature, thereby diminishing the YS of the quenched steel as per the Hall–Petch relation [18]. Secondly, the coarsened grains of the prior austenite and martensite blocks are susceptible to initiating micro-cracks during tensile tests, leading to intergranular fracture, and consequently reducing the EL [19,20].

Upon comparing S1050-550-550 and S1050-600-600, it is evident that as the pre-tempering and tempering temperatures increase, the EL also increases. Concurrently, the UTS and YS decreased significantly. This is linked to the aggregation and coarsening of the secondary carbides and decomposition of the tempered martensite induced by elevated tempering temperatures. Despite S1050-600-600 possessing high EL, the low YS severely hampers the application of the 5CrNiMoV steel.

Tempering is an effective method to modify precipitation behavior for enhancing the mechanical properties of die steels. By modulating the tempering conditions, S1050-600-550 exhibits exceptional mechanical properties, with an UTS of 1230 MPa, YS of 1120 MPa, and EL of 7.0%. Additionally, based on the aforementioned optimized parameters, the EL is further ameliorated with intercritical quenching. As delineated in Table 2, S1050L-600-550 boasts the highest EL of 8.2%, with an UTS of 1220 MPa and YS of 1110 MPa, showing better mechanical properties and can meet diverse engineering requirements.

3.3. Microstructures

Figure 8 illustrates the OM and SEM micrographs of S1100-550-550 and S1050-550-550, which have been quenched at varying temperatures. The microstructure is comprised of ferrite, tempered martensite, and secondary carbides. As shown in Figure 8a,b, a small amount of ferrite is distributed along the austenite grain boundaries, which is an important reference substance to measure the PAGS. Post-measurement, the PAGS of the specimens quenched at 1050 °C and 1100 °C are (156 ± 8) μm and (188 ± 16) μm, respectively. The migration ability of grain boundaries is enhanced at higher temperatures, thereby promoting grain growth. Consequently, the PAGS of S1100-550-550 is larger than that of S1050-550-550. During tempering, grain boundaries become the preferred nucleation sites for carbide precipitation [20]. Figure 8c,d reveals that the tempered martensite is composed of martensitic lath and secondary carbides. The secondary carbide size of S1050-550-550 is small (Figure 8c). Figure 8d demonstrates that with the rise in quenching temperature, the lath structure becomes more distinct due to the PAGS increase. Film-like carbides precipitate along the lath boundaries, forming numerous hard boundaries between the tempered martensite laths. Given that the hardness of the tempered martensite matrix is inferior to that of secondary carbides, the stress concentration at the lath boundaries intensifies during tensile deformation [21]. It causes micro-cracks to form and propagate along the lath boundaries, resulting in the swift fracture of S1100-550-550. Hence, the EL of S1100-550-550 is exceedingly low.

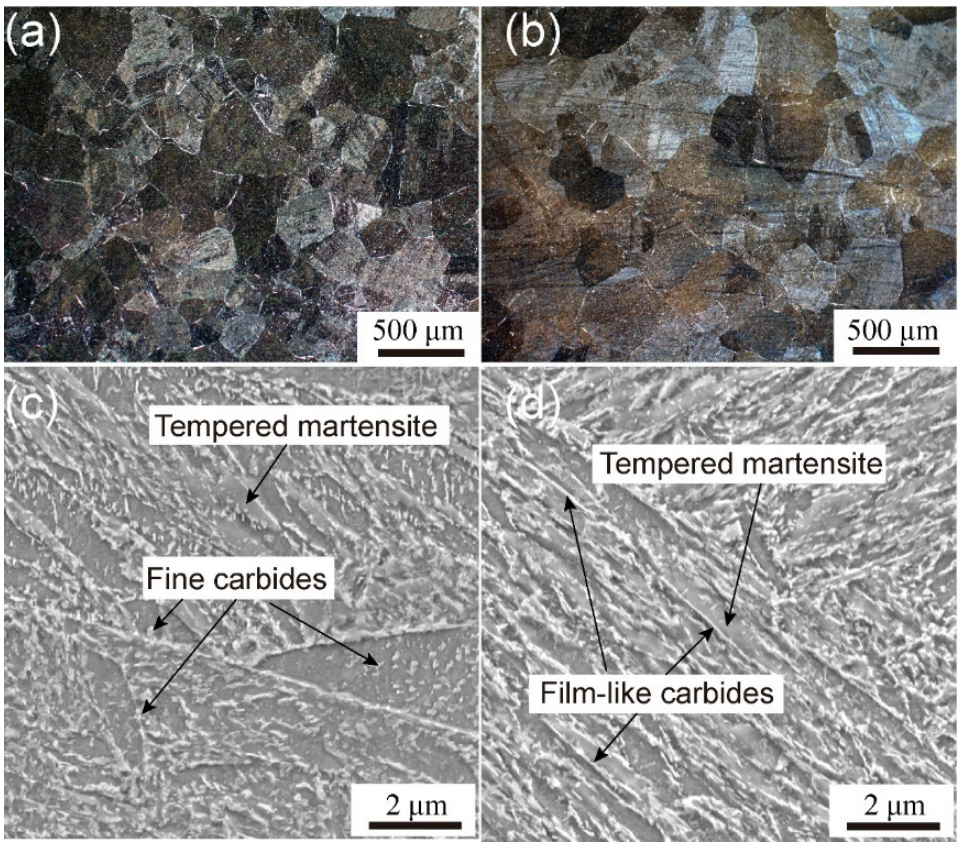

Figure 8. OM and SEM micrographs of the 5CrNiMoV steel. (**a**,**c**) S1050-550-550, and (**b**,**d**) S1100-550-550.

Figure 9 presents OM and SEM micrographs of S1050-600-600 and S1050-600-550, which have been tempered at different temperatures. Owing to the identical quenching temperatures, the average diameters of PAGBs of S1050-600-600 and S1050-600-550 are closely similar: (161 ± 10) μm and (165 ± 7) μm, respectively (Figure 9a,b). However, the morphology and average size of the secondary carbides vary with the tempering temperature. Figure 9c shows that when both the pre-tempering and tempering temperatures are 600 °C, the secondary carbides noticeably aggregated and coarse. Additionally, the decomposition of tempered martensite laths is also clearly observed. These factors contribute to a decline in the YS of S1050-600-600, which is 670 MPa. Figure 9d indicates that with a reduction in tempering temperature, the secondary carbide size significantly decreases. Furthermore, secondary carbides are observed not only along lath boundaries but also within martensitic laths. This suggests that pre-tempering at 600 °C promotes the precipitation nucleation of carbides. Subsequent tempering at 550 °C not only continues to promote precipitation, but also inhibits the coarsening of the carbides. Therefore, S1050-600-550 exhibits a favorable combination of ductility and strength (Figure 7).

Figure 10 displays OM and SEM micrographs of S1050L-600-550, which underwent intercritical quenching at 1050 °C, pre-tempering at 600 °C, and subsequent tempering at 550 °C. Figure 10a reveals that the microstructure of S1050L-600-500 consists of tempered martensite and pearlite. Due to intercritical quenching, only a portion of austenite is transformed into martensite, while the remainder is converted into pearlite during the subsequent tempering process. Figure 10b illustrates the interface of the tempered martensite and pearlite. The detailed structures of the tempered martensite and pearlite are shown in Figure 10c,d.

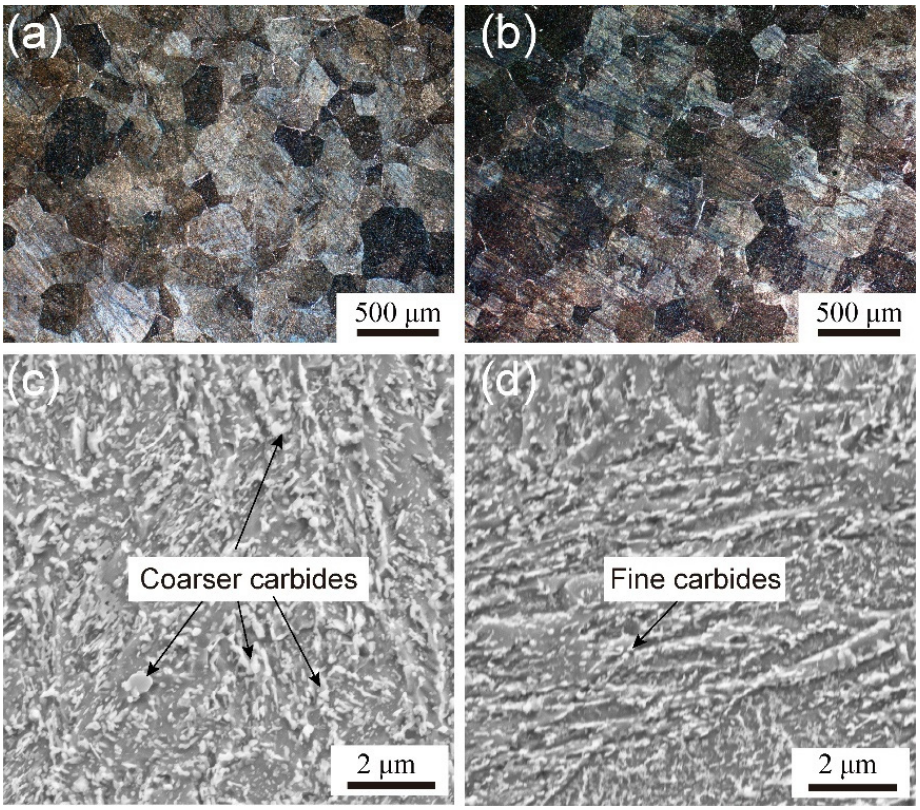

Figure 9. OM and SEM micrographs of the 5CrNiMoV steel. (**a**,**c**) S1050-600-600, and (**b**,**d**) S1050-600-550.

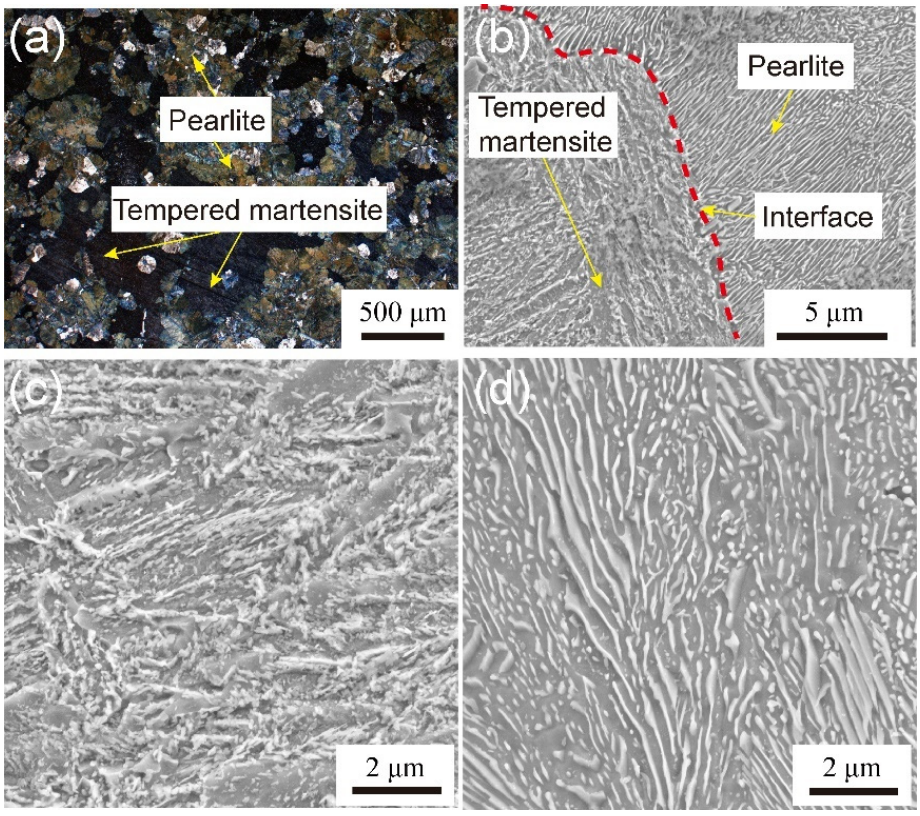

Figure 10. OM and SEM micrographs of S1050L-600-550. (**a**) Martensite and pearlite, (**b**) tempered martensite/pearlite interface, and detail of (**c**) tempered martensite, and (**d**) pearlite.

Figure 11 aims to quantitatively analyze the secondary carbides in 5CrNiMoV steel by counting the volume fraction and average size. As indicated in Figure 11a,b, S1050-600-550 achieves not only a high-volume fraction (26%) of the precipitated carbides, but also suppresses carbide coarsening ((0.12 ± 0.03) μm). Regarding other specimens, S1050-550-550 has the smallest average size of the secondary carbides, which is (0.09 ± 0.02) μm. However, the lower tempering temperature is not conducive to carbide precipitation. Thus, in S1050-550-550, the volume fraction of the secondary carbides is merely 11%. In S1100-550-550, the precipitation of a large number of strip-like carbides leads to an increase in both the average size and volume fraction of the secondary carbides. In S1050-600-600, the coarsened secondary carbides are caused by a higher tempering temperature, which is detrimental to the mechanical properties of die steel and should be avoided.

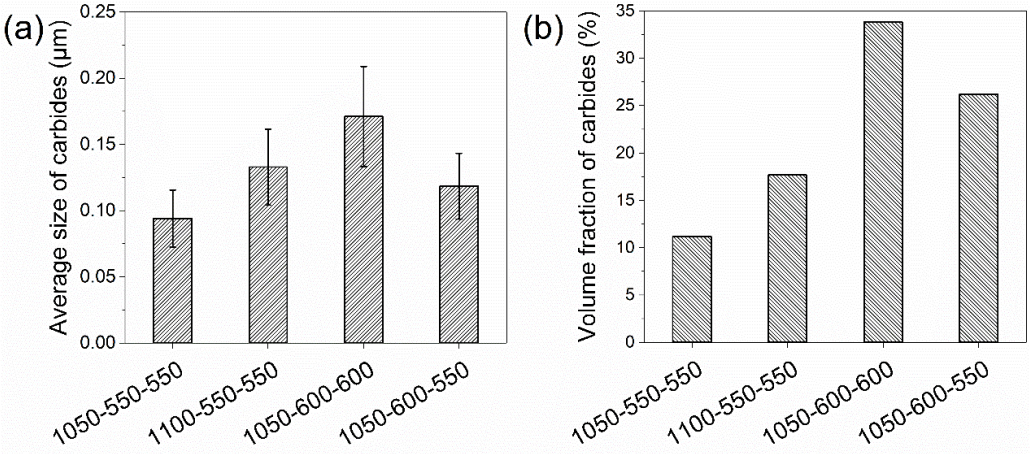

Figure 11. (**a**) Average size and (**b**) volume fraction of the secondary carbides.

3.4. Precipitation Strengthening

Due to the interaction of carbides and dislocations, precipitation strengthening is mainly related to the average size and volume fraction of the secondary carbides, which are important strengthening mechanisms of die steels [22]. According to the Ashby-Orowan model, the contribution to the YS ($\Delta\sigma_p$) of the secondary carbides is proportional to the 1/2 power of the volume fraction (f_p) and inversely proportional to the average size (d_p) of the secondary carbides [23]. It indicates that fine precipitates with fine grain size and high-volume fraction are beneficial for improving the contribution of precipitation strengthening to the YS of the 5CrNiMoV steel. The calculation formula of precipitation strengthening according to the Ashby–Orowan model is written as [23,24]:

$$\Delta\sigma_p = \frac{0.538Gbf_p^{\frac{1}{2}}}{d_p}\ln\left(\frac{d_p}{2b}\right) \quad (1)$$

where $\Delta\sigma_p$ is the contribution of YS caused by precipitation strengthening, G is the shear modulus of 5CrNiMoV steel (80.26 GPa), f_p is the volume fraction of the precipitated carbides, d_p is the average size of the precipitated carbides, and b is the Burgers vector.

Based on the information provided in Figure 11 regarding the volume fraction and average size of the secondary carbides, we have calculated the contribution of precipitation strengthening to the YS of different heat-treated specimens. Figure 12 illustrates that the contribution of precipitation strengthening to YS ranges from 190 MPa to 255 MPa. Among the specimens, S1050-600-550 exhibits the highest precipitation strengthening contribution, reaching 255 MPa. This finding is consistent with the observations made on the microstructure. Specimen 1050-600-550 possesses a higher volume fraction of secondary carbides and has a relatively fine carbide size, which results in a favorable combination of strength and ductility.

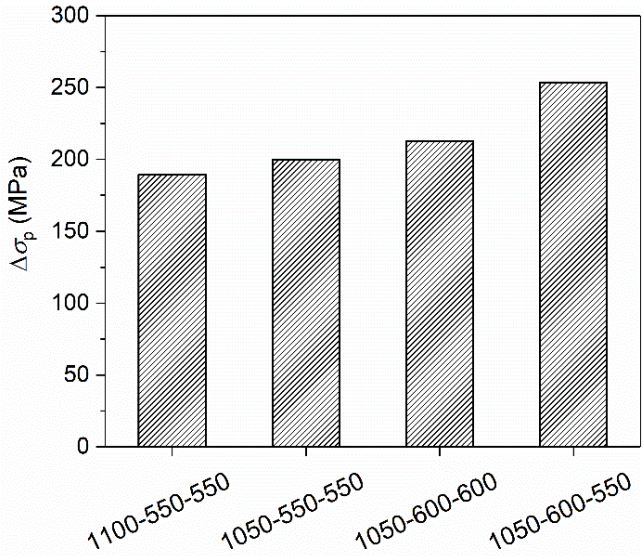

Figure 12. Contributions of precipitation strengthening to yield strength.

Figure 13 shows the XRD pattern of the heat-treated specimens. The results show that all the specimens are primarily composed of ferrite and martensite phases, and no obvious residual austenite peak is detected in the diffraction pattern.

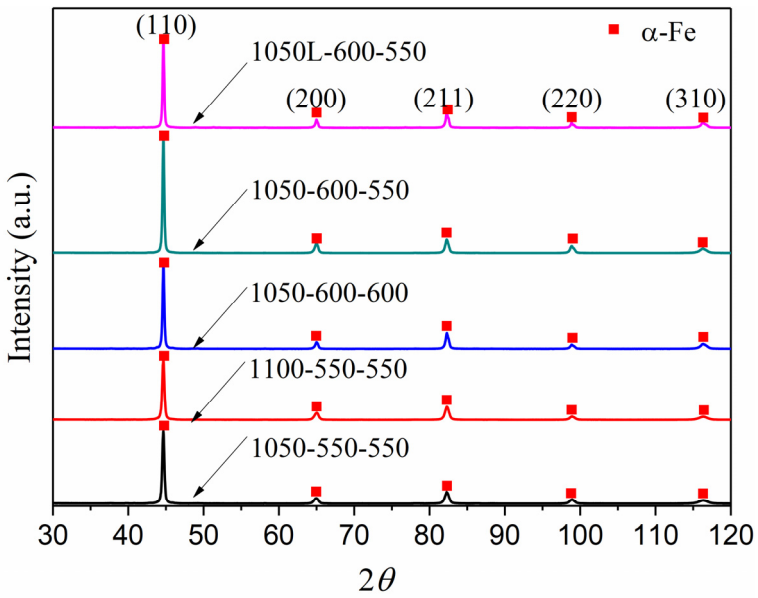

Figure 13. XRD patterns of the heat-treated specimens.

In the XRD analysis, the instrumental broadening has been corrected with the standard broadening data of polycrystalline Al_2O_3. The crystallite size and lattice strain affect the Bragg peak width. They are important parameters to determine mechanical properties. In the ferrite phase with BCC structure, the relationship between the lattice constant (a), the Miller indices ($\{h\ k\ l\}$), and the plane spacing (d) is shown as the following [25].

$$\frac{1}{d^2} = \frac{h^2 + k^2 + l^2}{a^2} \tag{2}$$

According to Bragg's law $\lambda = 2dsin\theta$ and Equation (2), the value of a is calculated by:

$$a = \frac{\lambda\sqrt{h^2 + k^2 + k^2}}{2\sin(\theta)} \tag{3}$$

where θ is the Bragg angle and λ is the X-ray wavelength.

As shown in Figure 14, the average values of the lattice constant for the heat-treated specimens range from 2.8669 to 2.8681 Å. Notably, the lattice constant value exhibits an inverse relationship with the volume fraction of the secondary carbides. This observation is consistent with the information presented in Figures 11b and 14, where it is evident that a higher volume fraction of secondary carbides corresponds to a smaller lattice constant. The increase in the volume fraction of secondary carbides with a decrease in the lattice constant can be attributed to the reduction in the content of solid solution alloying elements within the α-Fe matrix. As the volume fraction of secondary carbides increases, the amount of solid solution alloying elements decreases, leading to a reduction in lattice distortion. Consequently, the lattice constant decreases accordingly. In the case of S1050L-600-550, it undergoes intercritical quenching and tempering treatment, resulting in the formation of microstructures consisting of tempered martensite and pearlite. This specific heat treatment process promotes the precipitation of a significant number of carbides, leading to a smaller lattice constant.

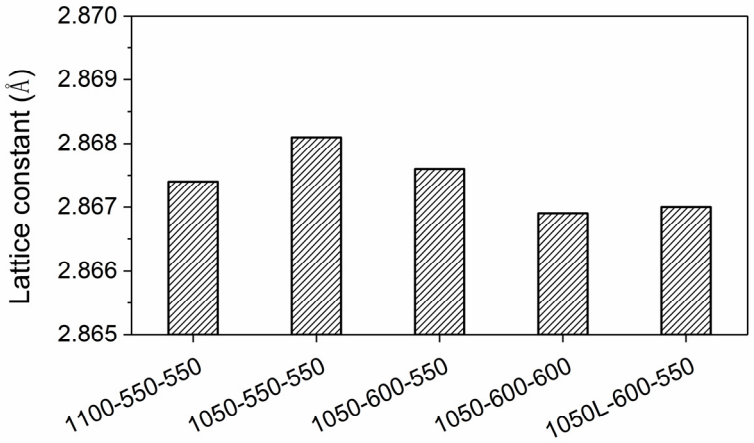

Figure 14. Lattice constant of the heat-treated specimens.

After obtaining the lattice constant, the average crystallite size is calculated using the Debye–Scherrer equation [26].

$$D = \frac{K\lambda}{\beta \cos\theta} \tag{4}$$

where θ is the Bragg angle, λ (0.154 nm) is the X-ray wavelength, β is the full width at half maximum (FWHM), and K is a constant equal to 0.89.

In addition, the lattice strain (ε) is determined according to the Williamson-Hall method [26,27]. Therefore, according to the results of average crystallite size and lattice strain, the dislocation density is calculated using the following equation [28–31].

$$\rho = \frac{2\sqrt{3}\varepsilon}{Db} \tag{5}$$

where ρ is the dislocation density, b is the Burgers vector—which for BCC metals, $b = (\sqrt{3}/2)a$—and a is the lattice constant as shown in Figure 14.

Figure 15 enumerates the computed values of the crystallite size, lattice strain, and dislocation density for all heat-treated specimens. The findings suggest that these parameters are significantly influenced by the pre-tempering temperature rather than the quenching temperatures. As shown in Figure 15a, the crystallite size increases with an increase in the pre-tempering temperature, while the lattice strain decreases. This reduction in lattice strain subsequently leads to a decrease in the dislocation density within the martensite matrix (Figure 15b,c). Furthermore, there is a negligible difference in the lattice strain, crystallite size, and dislocation density between S1050-600-550 and S1050-600-600.

This observation demonstrates that these parameters are predominantly influenced by the pre-tempering temperature. As shown in Figures 11b and 15, a higher pre-tempering temperature promotes the precipitation of carbides, thereby diminishing the lattice strain and dislocation density of the matrix, which is beneficial for enhancing the ductility of the 5CrNiMoV steel. Additionally, tempering following the pre-tempering process further enhances the precipitation of carbides. To prevent coarsening of the precipitated carbides, it is necessary to lower the tempering temperature. Consequently, in S1050-600-550, the higher volume fraction and finer size of secondary carbides (Figure 11) contribute to an increase in precipitation strengthening, leading to a relatively high YS. Moreover, the reduction in lattice strain and dislocation density also enhances the ductility of the specimen. Regarding S1050L-600-550, the primary microstructures present are tempered martensite and pearlite. Consequently, the values listed for the parameters in Figure 15 for S1050L-600-550 represent a combination of the characteristics exhibited by these two structures.

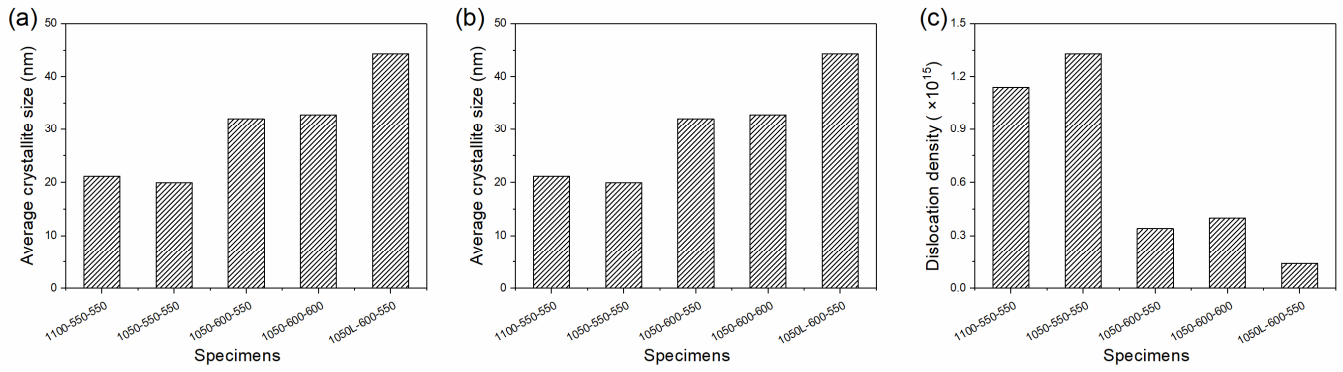

Figure 15. Average crystallite size (**a**), lattice strain (**b**), and dislocation density (**c**) of the heat-treated specimens.

3.5. Tensile Fracture

Figure 16 illustrates the tensile fracture morphologies of S1100-550-550 and S1050-550-550. As shown in Figure 16a and its detailed view in Figure 16b, the fractography of S1100-550-550 exhibits a brittle fracture model. As denoted by the yellow arrows, numerous micro-cracks are present on the cleavage facets, which contribute to crack propagation and fracture during tensile deformation [32–34]. Figure 16c,d reveals that, in addition to the intergranular fracture facets, local plastic deformation zones exist on the fracture surface. Consequently, there is a slight increase in the EL of S1050-550-550.

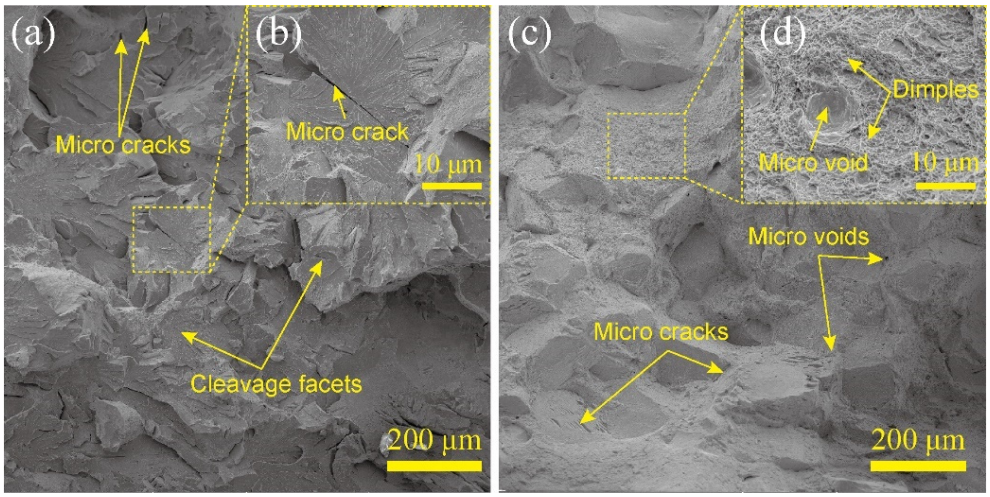

Figure 16. Fracture morphologies of (**a**,**b**) S1100-550-550 and (**c**,**d**) S1050-550-550.

Figure 17 presents the fracture morphologies of S1050-600-600 and S1050-600-550, characterized by a combination of ductile and brittle fractures. The fracture surfaces exhibit a multitude of intergranular facets, suggesting that brittle fracture is the predominant fracture model. However, as demonstrated in Figure 17a,c and their magnified views in Figure 17b,d, numerous fine dimples are visible, indicative of ductile fracture [34]. Therefore, S1050-600-600 and S1050-600-550 exhibit better ductility than S1050-550-550.

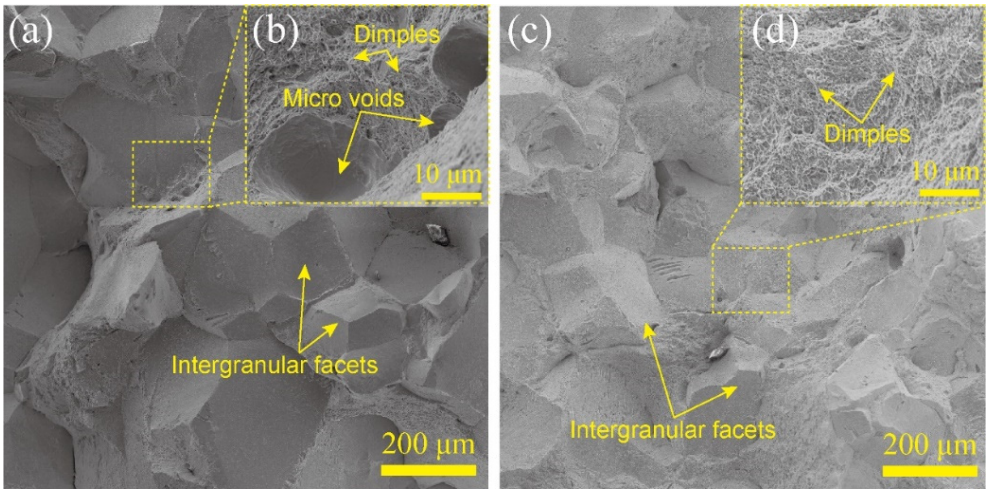

Figure 17. Fracture morphologies of (**a**,**b**) S1050-600-600 and (**c**,**d**) S1050-600-550.

Figure 18 displays the fracture morphology of S1050L-600-550, comprised of dimples, cleavage facets, and micro-cracks, and demonstrating a ductile-brittle mixed mode [32,35]. Furthermore, a notable increase in the number of dimples in Figure 18a compared to Figure 17a,c suggests a growing proportion of ductile fracture in S1050L-600-550. Additionally, as shown in Figure 18b, many deep dimples are formed by the pearlite during tensile deformation, which subsequently delays crack propagation and enhances the EL of the specimen. Therefore, S1050L-600-550 exhibits a relatively high EL.

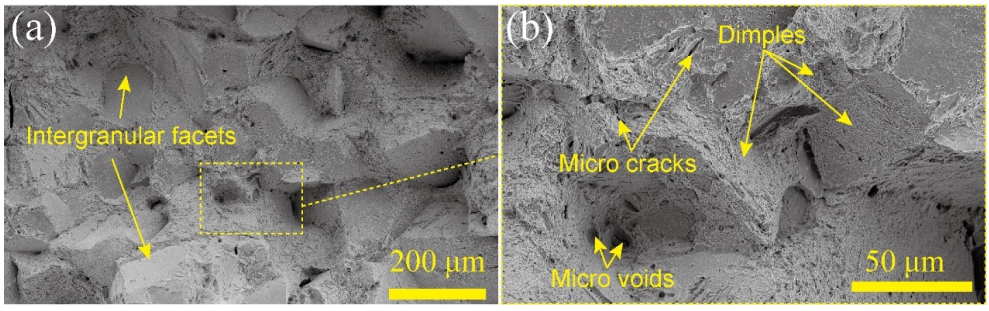

Figure 18. Fracture morphologies of S1050L-600-550. (**a**) Low magnification and (**b**) high magnification.

4. Conclusions

This study reveals that by controlling processing parameters, microstructures can be tuned to achieve comprehensive mechanical properties. The key conclusions are as follows:

(1) Proper heat treatment enhances the mechanical properties of 5CrNiMoV. A balance of strength and ductility is achieved with a UTS of 1230 MPa and an EL of 7.0% after quenching at 1050 °C, pre-tempering at 600 °C, and tempering at 550 °C. Furthermore, intercritical quenching at 1050 °C, pre-tempering at 600 °C, and tempering at 550 °C results in a higher EL of 8.2% with a UTS of 1220 MPa.

(2) Pre-tempering at 600 °C and tempering at 550 °C not only promotes the precipitation of carbides, but also inhibits their coarsening, effectively enhancing precipitation

strengthening and contributing to a 255 MPa increase in the YS. Additionally, the decrease in the solid solution of C and Cr elements in the α-Fe matrix due to increased carbide precipitation reduces the lattice micro-strain and dislocation density, thereby improving ductility.

(3) After intercritical quenching and tempering, the microstructure is composed of tempered martensite and pearlite. The high strength can be ascribed to the tempered martensite. The enhanced ductility is attributed to the decrease in micro-strain and dislocation density, as well as the mixed structures of tempered martensite and pearlite, which serve to hinder crack propagation during tensile deformation.

Author Contributions: W.H.: Methodology, Data curation, Visualization, Investigation, Writing—original draft, Writing—review and editing. L.L.: Project administration, Funding acquisition, Conceptualization. G.F.: Supervision, Conceptualization, Writing—review and editing. All authors have read and agreed to the published version of the manuscript.

Funding: This research was funded by the National Key Research and Development Program of China (grant number 2017YFB0701801).

Data Availability Statement: The data presented in this study are available within the article.

Conflicts of Interest: The authors declare no conflict of interest.

References

1. Huang, W.; Lei, L.; Fang, G. Microstructure evolution of hot work tool steel 5CrNiMoV throughout heating, deformation and quenching. *Mater. Charact.* **2020**, *163*, 110307. [CrossRef]
2. Hu, Z.; Wang, K. Evolution of Dynamic Recrystallization in 5CrNiMoV Steel during Hot Forming. *Adv. Mater. Sci. Eng.* **2020**, *2020*, 4732683. [CrossRef]
3. Jiang, W.; Wang, S.; Deng, Y.; Guo, X. Microstructure stability and high temperature wear behavior of an austenite aging steel coating by laser cladding. *Mater. Charact.* **2022**, *184*, 111700. [CrossRef]
4. Kundu, A.; Field, D.P. Influence of microstructural heterogeneity and plastic strain on geometrically necessary dislocation structure evolution in single-phase and two-phase alloys. *Mater. Charact.* **2020**, *170*, 110690. [CrossRef]
5. Dobrzanski, L.; Mazurkiewicz, J.; Hajduczek, E. Effect of thermal treatment on structure of newly developed 47CrMoWVTiCeZr16-26-8 hot-work tool steel. *J. Mater. Process. Technol.* **2004**, *157*, 472–484. [CrossRef]
6. Wang, H.; Li, J.; Shi, C.B.; Li, J.; He, B. Evolution of Carbides in H13 Steel in Heat Treatment Process. *Mater. Trans.* **2017**, *58*, 152–156. [CrossRef]
7. Yu, X.-S.; Wu, C.; Shi, R.-X.; Yuan, Y.-S. Microstructural evolution and mechanical properties of 55NiCrMoV7 hot-work die steel during quenching and tempering treatments. *Adv. Manuf.* **2021**, *9*, 520–537. [CrossRef]
8. Zhou, Q.; Wu, X.; Shi, N.; Li, J.; Min, N. Microstructure evolution and kinetic analysis of DM hot-work die steels during tempering. *Mater. Sci. Eng. A* **2011**, *528*, 5696–5700. [CrossRef]
9. Zhu, J.; Zhang, Z.; Xie, J. Improving strength and ductility of H13 die steel by pre-tempering treatment and its mechanism. *Mater. Mater. Sci. Eng. A* **2019**, *752*, 101–114. [CrossRef]
10. Kang, C.; Liu, F.; Jiang, Z.; Zhang, H.; Ding, S. Effect of nitrogen content on solidification behaviors and morphological characteristics of the precipitates in 55Cr17Mo1VN plastic die steel. *Mater. Charact.* **2022**, *194*, 112340. [CrossRef]
11. Sun, J.; Wang, H.; Xu, B.; Jiang, L.; Guo, S.; Sun, X.; Yu, D.; Liu, F.; Liu, Y. Making low-alloyed steel strong and tough by designing a dual-phase layered structure. *Acta Mater.* **2022**, *227*, 117701. [CrossRef]
12. He, B.B.; Hu, B.; Yen, H.W.; Cheng, G.J.; Wang, Z.K.; Luo, H.W.; Huang, M.X. High dislocation density-induced large ductility in deformed and partitioned steels. *Science* **2017**, *357*, 1029–1032. [CrossRef]
13. Li, Y.; Yuan, G.; Li, L.; Kang, J.; Yan, F.; Du, P.; Raabe, D.; Wang, G. Ductile 2-GPa steels with hierarchical substructure. *Science* **2023**, *379*, 168–173. [CrossRef] [PubMed]
14. da Silva, E.P.; Xu, W.; Fojer, C.; Houbaert, Y.; Sietsma, J.; Petrov, R.H. Phase transformations during the decomposition of austenite below M-s in a low-carbon steel. *Mater. Charact.* **2014**, *95*, 85–93. [CrossRef]
15. Shuai, J.; Zhao, J.; Lei, L.; Zeng, P.; Wu, X.; Sun, L. Characterization of crack propagation of Incoloy 800H by the combination of DIC and XFEM. *Nucl. Eng. Des.* **2020**, *364*, 110683. [CrossRef]
16. Ivanisenko, Y.; Wunderlich, R.; Valiev, R.; Fecht, H. Annealing behaviour of nanostructured carbon steel produced by severe plastic deformation. *Scr. Mater.* **2003**, *49*, 947–952. [CrossRef]
17. Cheng, T.; Wang, Y.; Zhao, Y.; Lv, L.; Hu, Q.; Ma, D. Effect of remelting solution heat treatment on microstructure evolution of nickel-based single crystal superalloy DD5. *Mater. Charact.* **2022**, *192*, 112186. [CrossRef]
18. Chen, J.; Kan, Q.; Li, Q.; Yin, H. Effects of grain size on acoustic emission of nanocrystalline superelastic NiTi shape memory alloys during fatigue crack growth. *Mater. Lett.* **2019**, *252*, 300–303. [CrossRef]

19. Rack, H. Role of prior austenite grain-size on the tensile ductility and fracture-toughness. *Scr. Metall.* **1979**, *13*, 577–582. [CrossRef]
20. Li, J.; Zhang, C.; Liu, Y. Influence of carbides on the high-temperature tempered martensite embrittlement of martensitic heat-resistant steels. *Mater. Mater. Sci. Eng. A* **2016**, *670*, 256–263. [CrossRef]
21. Du, N.; Liu, H.; Cao, Y.; Fu, P.; Sun, C.; Liu, H.; Li, D. In situ investigation of the fracture of primary carbides and its mechanism in M50 steel. *Mater. Charact.* **2022**, *186*, 111822. [CrossRef]
22. Wang, K.; Guo, Z.; Sha, W.; Glicksman, M.; Rajan, K. Property predictions using microstructural modeling. *Acta Mater.* **2005**, *53*, 3395–3402. [CrossRef]
23. Niu, T.; Kang, Y.L.; Gu, H.W.; Yin, Y.Q.; Qiao, M.L. Precipitation Behavior and Its Strengthening Effect of X100 Pipeline Steel. *J. Iron Steel Res. Int.* **2010**, *17*, 73–78. [CrossRef]
24. Gladman, T. Precipitation hardening in metals. *Mater. Sci. Technol.* **1999**, *15*, 30–36. [CrossRef]
25. Cullity, B.D.; Stock, S.R. *Elements of X-ray Diffraction*, 3rd ed.; Addison-Wesley Publishing: Boston, MA, USA, 2001.
26. Mote, V.; Purushotham, Y.; Dole, B. Williamson-Hall analysis in estimation of lattice strain in nanometer-sized ZnO particles. *J. Theor. Appl. Phys.* **2012**, *6*, 6. [CrossRef]
27. Sarkar, A.; Bhowmik, A.; Suwas, S. Microstructural characterization of ultrafine-grain interstitial-free steel by X-ray diffraction line profile analysis. *Appl. Phys. A* **2009**, *94*, 943–948. [CrossRef]
28. Zhao, Y.; Horita, Z.; Langdon, T.; Zhu, Y. Evolution of defect structures during cold rolling of ultrafine-grained Cu and Cu-Zn alloys: Influence of stacking fault energy. *Mater. Sci. Eng. A* **2008**, *474*, 342–347. [CrossRef]
29. Chen, J.; Lei, L.; Fang, G. Grain-size effects on the temperature-dependent elastocaloric cooling performance of polycrystalline NiTi alloy. *J. Alloys Compd.* **2022**, *927*, 166951. [CrossRef]
30. Sun, W.; Xu, C.; Qiao, X.; Zheng, M.; Kamado, S.; Gao, N.; Starink, M. Evolution of microstructure and mechanical properties of an as-cast Mg-8.2Gd-3.8Y-1.0Zn-0.4Zr alloy processed by high pressure torsion. *Mater. Sci. Eng. A* **2017**, *700*, 312–320. [CrossRef]
31. Zhao, Y.; Bingert, J.; Topping, T.; Sun, P.; Liao, X.; Zhu, Y.; Lavernia, E. Mechanical behavior, deformation mechanism and microstructure evolutions of ultrafine-grained Al during recovery via annealing. *Mater. Sci. Eng. A* **2020**, *772*, 138706. [CrossRef]
32. Huang, W.; Zhong, H.; Lei, L.; Fang, G. Microstructure and mechanical properties of multi-pass forged and annealed 42CrMo steel. *Mater. Sci. Eng. A* **2022**, *831*, 142191. [CrossRef]
33. Chen, J.; Yin, H.; Sun, Q. Effects of grain size on fatigue crack growth behaviors of nanocrystalline superelastic NiTi shape memory alloys. *Acta Mater.* **2020**, *195*, 141–150. [CrossRef]
34. Wang, J.; Zhao, Y.; Zhou, W.; Zhao, Q.; Huang, S.; Zeng, W. In-situ investigation on tensile deformation and fracture behaviors of a new metastable beta titanium alloy. *Mater. Sci. Eng. A* **2021**, *799*, 140187. [CrossRef]
35. Chen, X.; Zhao, G.; Xu, X.; Wang, Y. Effects of heat treatment on the microstructure, texture and mechanical property anisotropy of extruded 2196 Al-Cu-Li alloy. *J. Alloys Compd.* **2021**, *862*, 158102. [CrossRef]